Contribution of the Sub-Surface to Electrocatalytic Activity in Atomically Precise $La_{0.7}Sr_{0.3}MnO_3$ Heterostructures

Jegon Lee, Prajwal Adiga, Sang A Lee, Seung Hyun Nam, Hyeon-Ah Ju, Min-Hyong Jung, Hu Young Jeong, Young-Min Kim, Cindy Wong, Radwan Elzein, Rafik Addou, Kelsey A. Stoerzinger, and Woo Seok Choi**

J. Lee, Dr. S. A Lee, S. H. Nam, Prof. W. S. Choi
Department of Physics
Sungkyunkwan University
Suwon 16419, Republic of Korea
E-mail: choiws@skku.edu

P. Adiga, C. Wong, R. Elzein, R. Addou, Prof. K. A. Stoerzinger
School of Chemical, Biological and Environmental Engineering
Oregon State University
Corvallis, Oregon 97331, USA
E-mail: kelsey.stoerzinger@oregonstate.edu

Dr. S. A Lee
Department of Physics
Pukyong National University
Busan 48513, Republic of Korea

H.-A. Ju, M.-H. Jung, Prof. Y.-M. Kim
Department of Energy Science
Sungkyunkwan University
Suwon 16419, Republic of Korea

Prof. H. Y. Jeong
Central Research Facilities and School of Materials Science and Engineering
Ulsan National Institute of Science and Technology
Ulsan 44919, Republic of Korea

Prof. K. A. Stoerzinger
Physical Sciences Division, Pacific Northwest National Laboratory, Richland, Washington, 99254, USA

Keywords: electrocatalysis, oxygen evolution reaction, epitaxial oxide thin film, atomic scale precision, sub-surface layer

Electrocatalytic reactions are known to take place at the catalyst/electrolyte interface. Whereas recent studies of size-dependent activity in nanoparticles and thickness-dependent activity of thin films imply that the sub-surface layers of a catalyst can contribute to the catalytic activity as well, most of these studies consider actual modification of the surfaces. In this study, we investigate the role of a catalytically active sub-surface layers by employing atomic-scale thickness control of the $La_{0.7}Sr_{0.3}MnO_3$ (LSMO) films and heterostructures, without altering the catalyst/electrolyte interface. The activity of oxygen evolution reaction (OER) shows a non-monotonic thickness dependence in the LSMO films and a continuous screening effect in LSMO/$SrRuO_3$ heterostructures, which allowed us to define an "electrochemically-relevant depth" on the order of 10 unit cells. Our study on the electrocatalytic activity of epitaxial heterostructures provides new insight in designing efficient electrocatalytic nanomaterials and core-shell architectures.

1. Introduction

The quest to maximize catalytic activity of oxide catalysts for the oxygen evolution reaction (OER) strives to compare "intrinsic activity" normalized by the available active sites.[1-4] These active sites are generally understood to be undercoordinated transition metals located at the surface.[5-13] In some cases, the redox of these metals during cycling, such as in RuO_2[14] and Ni-based oxides,[15] can be used to estimate their surface concentration. The density of active sites is often simply approximated by the exposed geometric surface area (measured by e.g. microscopy or N_2 adsorption[16]) or the electrochemical surface area (ECSA) by assumptions regarding intrinsic capacitance.[15,17-19] However, all of these normalization approaches imply that electrochemical activity is governed exclusively by the terminal surface layer of the oxide, without serious consideration of sub-surface layers that may influence activity as well.

Size effects in the OER activity of nanoparticles,[20,21] thickness-dependent effects in thin films,[22] and substrate-dependent effects in two dimensional materials[23] imply that while a catalytic reaction occurs at the catalyst/electrolyte interface, the supporting layers of a catalyst (and/or its support) can influence activity as well. For oxides, these size effects can include manipulating the ability of transition metal sites to oxidize prior to the onset of OER.[20,21] Thickness effects can additionally include charge transfer to/from a support,[24-26] quantum tunneling though ultra-thin layers,[27,28] and formation of a depletion layer.[29] Thickness-dependent strain effects in thin films might also lead to corresponding changes to the electronic structure, impacting activity.[30-33] Missing, however, is a systematic understanding of how the thickness of a conductive oxide can impact OER activity and how such trends might depend on the nature of the underlying support.

Recent works have further demonstrated that on some highly covalent oxides, the sub-surface layers of an electrocatalyst may play a role when the OER mechanism involves exchange of lattice oxygen with the electrolyte.[34] In epitaxial thin films that remain crystalline during OER cycling, such as in $LaNiO_3$ thin films, the extent of the direct oxygen exchange is estimated to be ~2 nm (around 5 unit cells).[35] Thus, one might expect that activity depends not only on the terminal layer chemistry and electronic structure, but that of the sub-surface layers as well. Even more dynamic lattice oxygen involvement is observed in other materials that become amorphous upon cycling, such as $Ba_{0.5}Sr_{0.5}Co_{0.8}Fe_{0.2}O_{3-\delta}$,[34] for which water has been observed to dissociate within the lattice itself to form bubbles of oxygen and hydrogen gas.[36] For $LaMnO_{3+\delta}$, the dependence of capacitance on scan rate, *p*H, and electrolyte has led to the suggestion that OH^- can intercalate into the lattice.[37] Thus, several potential mechanisms for involvement of the sub-surface activity in OER may be possible. However, the extent of their impact on activity is yet to be understood through control of electrocatalyst thickness with atomic-scale precision.

To scrutinize the role of the sub-surface layers in OER, we propose the concept of an electrochemically-relevant depth (t_{ec}), and a method to determine it. As schematically shown in **Figure 1**, we presume that the electrochemically-relevant sites, herein defined as those that influence the oxidative current under OER conditions, can extend over several unit cells in thickness of a crystalline sample. For an active film "A" on an inactive substrate, a film thickness (t_A) less than t_{ec} would then exhibit reduced activity compared to one of thickness t_{ec}, with greater thickness still showing the same activity normalized to the exposed geometric surface area (Figures 1a-1c). On the other hand, it is also possible to examine a heterostructure consisting of a catalytic layer "A" on top of a significantly more active catalytic layer "B", where the interaction between these layers improves the resultant activity for thinnest films. For this heterostructure, as t_A approaches t_{ec}, the effect of these interactions would be more screened, eventually reaching the intrinsic activity of layer "A" for thicknesses greater than t_{ec} (Figures 1d-1f). A thickness-dependent electrocatalytic study with atomic-scale precision at the ultra-thin limit would assess this hypothesis and determine t_{ec}.

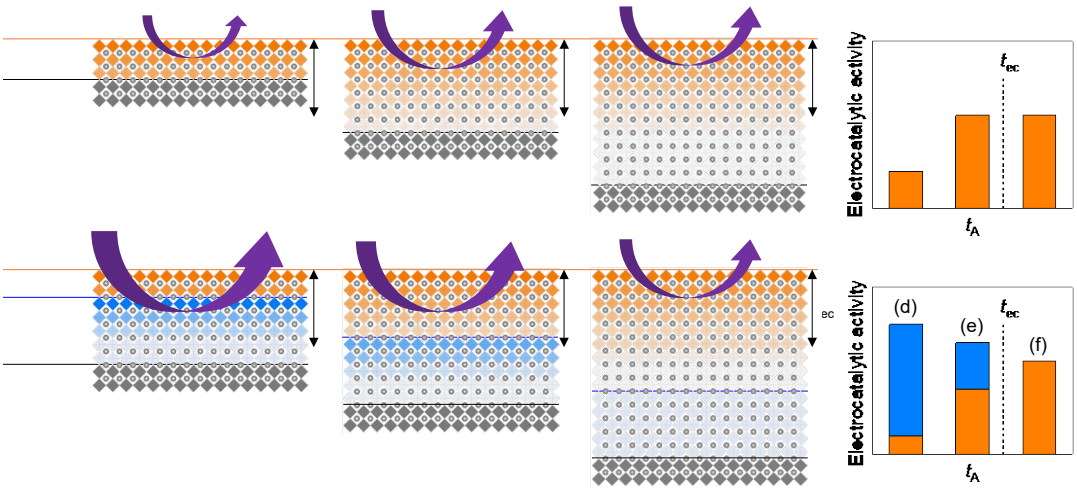

Figure 1. Schematic representations of the electrochemically-relevant depth in different heterostructure geometries. Vertical distribution of electrochemically active sites and the electrocatalytic activity in (a-c) film A//substrate and (d-f) film A (less active)/film B (more

active)//substrate geometries. For both cases, the atomic thickness of film A (t_A) is controlled in the ultra-thin limit, for (a,d) thinner than t_{ec}, (b,e) comparable to t_{ec}, and (c,f) thicker than t_{ec}. The size of the purple curved arrows indicates the electrochemical activity, which are also plotted as bar graph on the right.

In this study, we control the thickness of epitaxial $La_{0.7}Sr_{0.3}MnO_3$ (LSMO) thin films with atomic-scale precision using pulsed laser epitaxy (PLE) and study its impact on oxygen electrocatalysis. LSMO represents a model conductive oxide with moderate activity in alkaline media (layer A in Figure 1),[25,38] and is a half-metal, in contrast to other insulating or semiconducting films that have previously demonstrated thickness-dependent activity.[25,31] We compare the activity for LSMO thicknesses ranging from 2 to 70 unit cells (u.c., where the *c*-axis lattice parameter is ~3.88 Å) grown on two supports: bare Nb (0.5wt%) doped (001) $SrTiO_3$ (NSTO) substrates (LSMO//NSTO) and $SrRuO_3$ (SRO, fixed to 5 nm) covered NSTO substrates (LSMO/SRO//NSTO). NSTO is a degenerately doped *n*-type semiconductor, whereas SRO is metallic. While NSTO is inactive for OER,[26] SRO exhibits significantly higher electrocatalytic activity compared to the LSMO (but is unstable) (layer B in Figure 1).[39-41] On NSTO, LSMO activity continuously increases with the thickness, up to ~7 u.c., but further gradually until ~23 u.c., suggesting the sub-surface layers do influence the OER activity. The activity decreases for thicker films, for which bulk charge transfer resistances contribute for thicknesses > 50 u.c. On SRO, LSMO shows greatest activity for thinnest films, showing bulk LSMO-like behavior for thicknesses > 20 u.c. Compared to metals where electronic substrate effects (and by extension, core-shell effects in nanoparticles) are limited to adjacent layers (e.g. Pt/Cu),[42] these findings highlight the increased length scales over which a buried layer may play a role during electrocatalysis on metal oxides, even when these oxides are metallic in nature. Furthermore, these findings indicate that the electronic structure of the top ~10 u.c. of oxides do impact the OER activity,

and in some cases these layers may even be actively involved in OER via ionic transport through the oxide lattice, comprising the concept of t_{ec}.

2. Result and Discussion

The unit-cell level control of the LSMO film thickness was demonstrated from X-ray diffraction (XRD) measurements, as shown in **Figures 2a-2d**. The epitaxial films are phase pure in the full θ-2θ scans and high-quality evidenced by the low full-width-half-maximum (FWHM) values in the rocking-curve scans (see Figures S1 and S2, Supporting Information). As the film thickness increased, the LSMO (002) Bragg peak systematically increased in intensity (Figures 2a and 2c), and the interference fringes became more closely spaced, as expected. The thickness of each film was identified from X-ray reflection (XRR) measurements (Figures 2b and 2d). For some selected samples, thicknesses were confirmed by scanning transmission electron microscopy (STEM) images. We further note that LSMO, NSTO, and SRO layers are all well lattice matched with the same in-plane lattice constants, negating epitaxial strain as a primary player in thickness-dependent effects, at least up to the thicknesses used in the study (the reported thickness of strain relaxation for LSMO is ~100 nm).[43] Indeed, all the samples were fully strained with tetragonal crystal structures, as confirmed by the XRD reciprocal space mapping measured at different ϕ angles (Figures S1c and S2b, Supporting Information). STEM measurements with energy-dispersive X-ray spectroscopy further certify the uniform and sharp epitaxial interfaces with atomic-scale precision, conformal thickness, and lack of elemental mixing in our samples (Figures 2e-2i). Noting that the surface Mn contents has been shown to correlate with the electrocatalytic activity,[13, 44] our LSMO thin film showed the uniform Mn stoichiometry throughout it's thickness, consistent with previous work,[45] suggesting the surface composition may be similar regardless of thicknesses measured here.

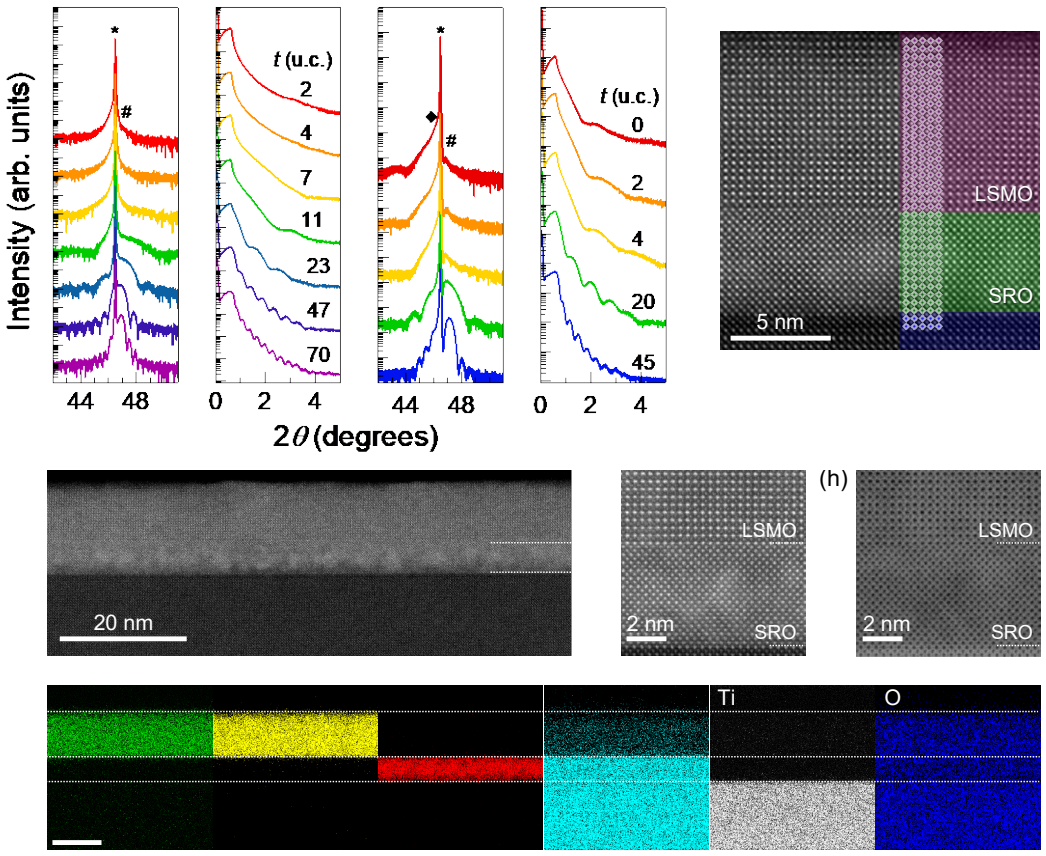

Figure 2. Atomic-scale precision control of the thickness of LSMO epitaxial thin films and heterostructures. (a,c) XRD θ-2θ scans and (b,d) XRR of the (a,b) LSMO/NSTO thin films and (c,d) LSMO/SRO//NSTO heterostructures. *, #, and ♦ in (a) and (c) indicate the (002) Bragg peaks of the NSTO substrate, LSMO film, and SRO layer, respectively. (e) STEM images for the atomic-scale precision control of the thickness. High-resolution high-angle annular dark-field STEM of the heterostructures with (f) low- and (g) high-magnification, and the (h) annular bright-field STEM indicate that the interfaces are well-defined. (i) The elemental images using energy dispersive X-ray spectroscopy clearly identify all the layers in the heterostructure in atomic scale, against any cation intermixing at the interface.

The intrinsic OER activities of epitaxial LSMO thin films (LSMO (*t* u.c.)//NSTO) in 0.1 M KOH, measured by cyclic voltammetry (CV), showed a non-monotonic *t*-dependent behavior.

Figure 3a shows the geometric area (GA)-normalized CV results, subtracting the capacitive current estimated from the forward sweep averaged from 1.40-1.45 V vs. RHE (Figure S3, Supporting Information). Owing to consistent layer-by-layer growth and an atomically smooth surface, the same *t*-dependent trend was consistently obtained when the currents were normalized by the ECSA from the double layer capacitance (See Supplementary Note #1, Figures S4-S7, and Table S1, Supporting Information). The specific current densities (i_s @ 1.65 V vs. RHE) from the CV curves (Figure 3a) and the Tafel slopes (β) from the Tafel plots (Figure 3b) are summarized in Figure 3c, Table S2, and Supplementary Note #2, Supporting Information. Whereas the OER onset overpotential (η_{on}) values are independent of *t* (~0.4 V) (Figure S8, and also Table S2, Supporting Information), i_s increased up to t = 23 u.c. and then decreased. This is oppositely shown for β, while the trend is somewhat suppressed. β is large (> 80 mV dec^{-1}) for the thinnest and the thickest films but otherwise comparable (~52 mV dec^{-1}, Table S2, Supporting Information). To describe the surprising non-monotonic *t*-dependent activity trend in i_s and β, three different *t*-regions were identified: (1) drastically increasing ($0 < t <$ ~7 u.c., red), (2) gradually increasing (~7 $< t <$ ~25 u.c., green), and (3) decreasing ($t >$ ~25 u.c., yellow) regions are marked in Figure 3c. The higher value of β for the thinnest (2 u.c.) and thickest (70 u.c.) LSMO films indicate reduced charge transfer kinetics. In these thin- and thick-limits (regions (1) and (3), respectively), the reduced charge transfer kinetics would strongly hamper the OER activity. For example, comparing perovskite powders dispersed with conductive carbon, the Tafel slope increased with decreasing bulk conductivity.[3]

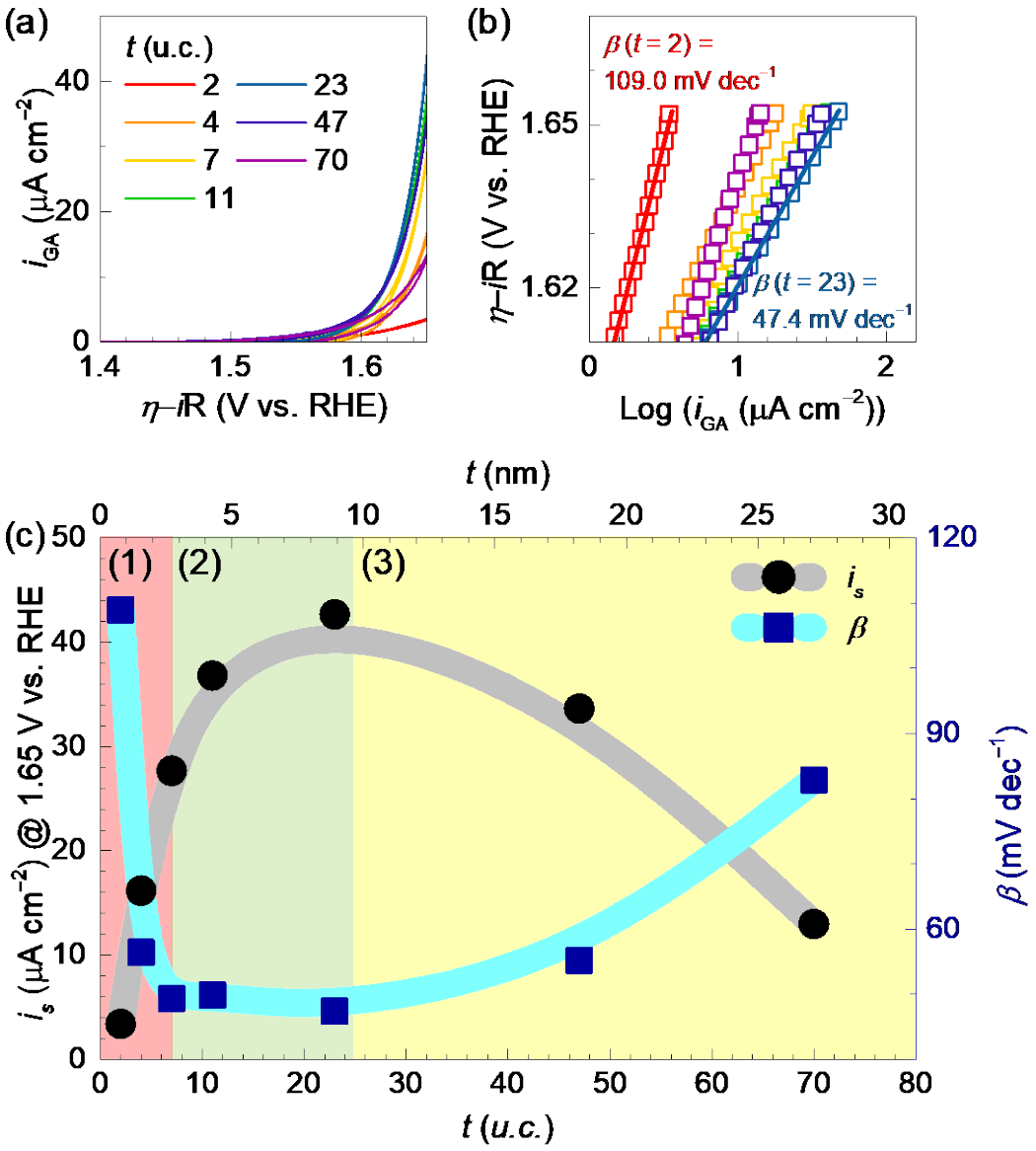

Figure 3. *t*-dependent oxygen evolution reaction in the ultra-thin limit. (a) OER cyclic voltammetry and (b) its Tafel plots. (c) Summary of the specific current densities of the OER (i_s) at a potential of 1.65 V vs. RHE (left axis) and Tafel slopes of the OER (β) (right axis) as a function of t. The t = 23 u.c. (~10 nm) LSMO thin film shows the highest OER activity. Regions (1), (2) and (3) are marked as red, green, and yellow, respectively (see the main text).

To better understand the reduced charge transfer kinetics of LSMO in *t*-regions (1) and (3), we performed a facile redox reaction using $[Fe(CN)_6]^{3-/4-}$, as shown in Figure S9, Supporting Information. This outer sphere redox couple has comparable reversible potential to OER,

enabling characterization of charge transport under reaction conditions. In *t*-region (1), the thinnest films (2 and 4 u.c.) show notably large resistance to charge transfer, reflected in the increased peak separation ΔE_p (Figure S9, Tables S3-S5, Supporting Information). These films also exhibit a reduced peak height, i_p, implying a critical thickness of ~7 u.c. is required to reach similar electron conductivity in LSMO thin films. Indeed, the electric resistivity of the LSMO thin films drastically increases with decreasing film thickness attributed to an ultra-thin insulating LSMO dead layer (~6 u.c.), which is formed at the film/substrate interface possibly due to unintentional increase of Sr concentration (Figure S10).[45-48] This insulating layer would result in reduced charge transport under OER conditions, limiting activity. Above this critical thickness (*t*-region (2)), films exhibit similar transport properties measured in-situ by the $[Fe(CN)_6]^{3-/4-}$ redox couple. On the other hand, for the thick films (*t*-region (3)), the charge transport (in parallel with OER activity) is again hindered, but because of a completely different origin. Here, the reduced charge transport is likely associated with the longer vertical path for the electrons in the LSMO layer, also evidenced by increased surface recombination time above 25 u.c.[49] A similar effect has been observed with increasing thickness (10-40 nm) of $LaCoO_3$ thin films.[31] Hence, the *t*-dependent activity trends of *t*-regions (1) and (3) can be understood by reduced charge transfer kinetics.

Surprisingly, in the *t*-region (2), the OER activity of LSMO thin films continues to increase gradually from 7 to 23 u.c., despite the consistent charge transfer resistance by $[Fe(CN)_6]^{3-/4-}$ redox. Together with the lesser increase in activity for a given increase in film thickness compared to that of *t*-region (1), we thus propose that the electronic structure of the sub-surface layer influences the OER activity. This influence may be indirect, such as manipulating the ability of the lattice to exchange oxygen with the electrolyte, or direct by catalyzing OER in the sub-surface layers should ionic transport be appreciable, and its extent

(both in magnitude and length scale) likely depends on the chemistry of the oxide electrocatalyst and the electrolyte as well.

We next look to leverage this influence of sub-surface layers on OER activity via a thickness-controlled LSMO overlayer on a more active but unstable catalyst, SRO. η_{on} on SRO thin films is close to the thermodynamic potential (η_{on} < ~0.2 V),[39-41] just beyond that of Ru oxidation and significantly lower than that of LSMO (η_{on} = ~0.4 V). One can expect that an epitaxial heterostructure of LSMO (*t* u.c.)/SRO//NSTO will exhibit OER activity in between SRO and LSMO, given our proposal that the electronic structure modification of sub-surface layers of LSMO influences the OER activity.

We performed CV measurements with gradually increasing anodic potential to systematically determine the η_{on} of the heterostructures while minimizing degradation of the unstable SRO layer. The first CV scan was obtained up to ~1.45 V vs. RHE, and then, in the following scans, the maximum potentials were systematically increased with an interval of 0.05 V, as shown in Figure S11, Supporting Information. Among the CV curves, the curves having the highest maximum current density were selected for each sample and plotted in Figure 4a. η_{on} values of the LSMO/SRO//NSTO heterostructures are plotted in Figure 4b, along with those of the LSMO//NSTO thin films.

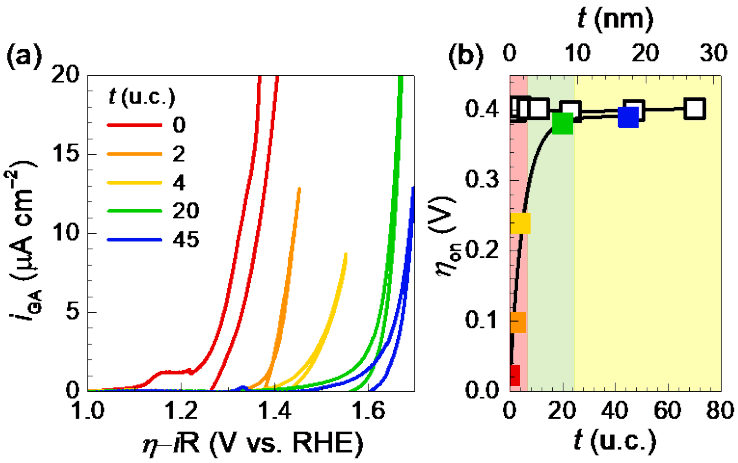

Figure 4. The contribution of sub-surface layers to OER activity in LSMO/SRO//NSTO heterostructures. (a) Cyclic voltammetry curves of the LSMO (*t* u.c.)/SRO (13 u.c.)//NSTO heterostructures. (b) *t*-dependent η_{on}. The open squares show η_{on} of the LSMO//NSTO thin films obtained from Figure 3a. The corresponding thickness regions from Figure 3 are also indicated in colors.

The presence of an underlying SRO layer strongly influences the OER of the heterostructure. First, we confirm that the presence of SRO layer within the heterostructures does not alter the layer-by-layer growth and resultant atomically smoothness (and full coverage) of the LSMO surface evidenced by atomic force microscopy (Figures S6c and S6d, Supporting Information). Nevertheless, the Ru redox features were still observed prior to the onset of OER for LSMO (2 u.c.)/SRO//NSTO heterostructures at ~ 1.12 V vs. RHE (Figures S10b, Supporting Information), although to a lesser extent than on SRO only.[39] In addition, despite the presence of the LSMO overlayer, the activity of thin LSMO/SRO//STO heterostructure degrades with extended cycling, which may be activated by the Ru redox process or ionic transport within the lattice. These results suggest that Ru interacts strongly with the LSMO lattice oxygen, or that OH^- species might penetrate through films on these length scales,[37,50] allowing the buried SRO layer to more actively participate in OER.

With increasing LSMO *t*, a systematic increase of the η_{on} was observed for the LSMO/SRO//NSTO heterostructures in the *t*-region (1) and (2). This *t*-dependent trend of the activity is consistent with the expectation in Figures 1d-1f, as the high OER activity of SRO was gradually shielded by the less active LSMO layer. The trend continues up until t_{ec}, where the heterostructure shows comparable electrochemical characteristics to the LSMO layer alone. Likewise, the electrochemical impedance spectroscopy for the ultra-thin LSMO films (≤ 13 u.c.) clearly exhibits reduced charge transfer resistance with low applied potentials around those of Ru redox features, as shown in Figure S12, Supporting Information. Thus, in the *t*-regions (1) and (2), improved OER activity can be mainly attributed in part to enhanced charge transfer properties compared to bare LSMO films of comparable thickness on NSTO, but additionally to beneficial charge interaction with the SRO layer, given that the heterostructure activity exceeds that of thick LSMO films (where OER activity saturates).

We next compare these LSMO/SRO//NSTO heterostructures to those in literature employing a wide band-gap insulator, STO, as SRO capping layer. While in both cases, the heterostructure exhibits enhanced activity compared to a 2 u.c. catalyst film (LSMO and STO) without the SRO layer, the activity of LSMO (2 u.c.)/SRO//NSTO (η_{on} ~0.1 V) is notably higher than the activity of STO (2 u.c.)/SRO//NSTO (η_{on} ~0.4 V).[26] These results further imply that the nature of the catalyst surface, even when modulated by electronic interaction with a buried layer, drives the rate of reaction. The reduction in LSMO/SRO//NSTO activity with cycling, however, suggests that thin layers (2 and 4 u.c.) may not be sufficient to prevent Ru dissolution in a mechanism yet-to-be understood. X-ray photoelectron spectroscopy suggests the LSMO film remains on the surface of the 4 u.c. LSMO/SRO//NSTO heterostructure post-cycling, albeit with a higher Mn/La ratio (2.28, accounting for elemental cross-sections) than expected (1.43) and compared to a thicker 20 u.c. LSMO/SRO//NSTO heterostructure (1.39), potentially indicating Sr segregation at the LSMO/SRO interface

(Figure S10, Supporting Information). However, Ru in the 4 u.c. LSMO/SRO//NSTO heterostructure is substantially depleted (Figure S13, Supporting Information). As such, the oxidative current on the heterostructures at low overpotentials likely includes a large component from lattice oxygen evolution during Ru dissolution. The ability for thin LSMO layers to permit oxidation at an underlying layer, while detrimental in this case, may be beneficial for controlling selective oxidation processes in complex electrolytes, such as seawater electrolysis.

3. Conclusion

We examined the thickness dependent electrocatalytic activities of epitaxial LSMO thin films and LSMO/SRO heterostructures in the ultra-thin limit of the LSMO layer, and determined that films exhibit activity influenced by underlying sub-surface layers. When supported on an inactive NSTO substrate, OER activity was reduced on thin LSMO films, whereas support on an SRO//NSTO heterostructure promoted oxidation current due to the facile evolution of oxygen on SRO. The length scales over which activity is modulated suggest that the top layers, on the order of 10 u.c., of LSMO influence OER, either directly (e.g. by the involvement of lattice oxygen in the mechanism or OH^- diffusion) or indirectly (e.g. by electronic structure). Together, these findings suggest additional routes to understand and improve catalytic activity by adopting core-shell morphologies or conformal coatings.

4. Experimental Section/Methods

Epitaxial heterostructure growth and X-ray diffraction: We employed pulsed laser epitaxy using KrF excimer laser (248 nm, Lightmachinery). The growth temperature, repetition rate, laser fluence, and oxygen partial pressure were 750°C, 2 Hz, 1.52 J cm^{-2}, and 100 mTorr for all the samples, respectively. We used the sintered ceramic targets of LSMO and SRO with pseudo-cubic lattice parameters of 3.876 Å and 3.926 Å, respectively for ablation. (001)

NSTO (0.5wt% Nb) single crystals were used as substrates. The thicknesses of thin films were precisely controlled using the number of laser pulses during growth and later double-checked by X-ray reflectivity (XRR). High-resolution X-ray diffractometer (XRD, Malvern Panalytical, X`Pert MRD) was used to characterize the crystalline quality and lattice structures of both epitaxial LSMO thin films and LSMO/SRO heterostructures grown on NSTO substrates, via XRR, θ-2θ scans, rocking curve scans, and reciprocal space mapping.

Atomic structural characterization: Cross-sectional samples of the epitaxial LSMO/SRO heterostructures were prepared by focused Ga ion beam milling and slicing method using a dual-beam focused ion beam system (FIB, Helios NanoLab 450, Thermo Fisher Scientific). The subsequent low energy Ar ion beam milling at 900 V for 15 min (Fischione Model 1040 Nanomill) was applied to the thin samples as post treatment to remove the damaged surface layer that can be caused by heavy Ga ion beam milling. Atomic-resolution high-angle annular dark field (HAADF) and annular bright field (ABF) images of the thin films were taken on a 200-kV aberration-corrected scanning transmission electron microscopy (STEM, JEM-ARM200CF, JEOL Ltd., Japan) with an electron probe size of 0.8 Å and semi-convergence angle of 23 mrad. The angle ranges of the HAADF and ABF detectors were set to 70-175 mrad and 12-23 mrad, respectively. Nanoscale elemental maps of the heterostructures were obtained via energy-dispersive X-ray spectroscopy (EDX, JED-2300T, JEOL) using a dual-type silicon drift detector with a large effective solid angle (~1.2 sr) in the STEM mode.

Electrocatalytic properties: Electrochemical measurements were performed on VSP-300 (Biologic potentiostat). The LSMO/NSTO and LSMO/SRO/NSTO electrodes were back contacted with Ti wire, and a good electrical contact was ensured by applying Ga-In eutectic (to overcome any Schottky barrier) and silver paste. For electrochemical measurements, a 50 mL single PTFE® compartment three-electrode setup containing 0.1M KOH (Sigma-Aldrich)

was prepared with 18.2 MΩ Millipore water. Ag/AgCl electrode (CH Instruments, Inc.) corrected to RHE in the same electrolytes was used as the reference electrode. A Pt wire (CH Instruments, Inc.) was used as a counter electrode and cleaned with aqua-regia prior to each run. Cell and cell components were stored in 1:4 HCl:H_2O overnight between experiments to dissolve any metal contaminant from a previous run and rinsed thoroughly with Millipore water before use. ECSA measurements were performed in N_2 saturated environment in the non-Faradaic region. All other measurements were performed in O_2 (UHP Gr. 4.4) saturated conditions with the scan rate of 5 mV s^{-1}. Applied potentials were *iR* compensated.

Supporting Information
Supporting Information is available from the Wiley Online Library or from the author.

Acknowledgements

J.L. and P.A. contributed equally to this work. This research was supported by the Basic Science Research Programs through the National Research Foundation of Korea (NRF-2021R1A2C2011340, NRF-2019R1A2C1005267 (S.AL.), and NRF-2020R1A2C1006207 (Y.-M.K.)). K.A.S. acknowledges support from Oregon State University as a Callahan Faculty Scholar. P.A. acknowledges support from the Link Foundation Energy Fellowship. Part of this research was conducted at the Northwest Nanotechnology Infrastructure, a National Nanotechnology Coordinated Infrastructure site at Oregon State University which is supported in part by the National Science Foundation (grant NNCI-2025489) and Oregon State University. Acquisition of the Ambient-Pressure X-ray Photoelectron Spectroscopy/Ambient-Pressure Scanning Tunneling Microscopy system was supported by the National Science Foundation-Major Research Instrumentation program (grant DMR-1429765), the M. J. Murdock Charitable Trust, Oregon BEST, Oregon Nanoscience and Microtechnologies Institute, and Oregon State University.

Received: ((will be filled in by the editorial staff))
Revised: ((will be filled in by the editorial staff))
Published online: ((will be filled in by the editorial staff))

References

[1] J. Suntivich, K. J. May, H. A. Gasteiger, J. B. Goodenough, Y. Shao-Horn, *Science* **2011**, *334*, 1383.

[2] M. K. Debe, *Nature* **2012**, *486*, 43.

[3] W. T. Hong, K. A. Stoerzinger, Y.-L. Lee, L. Giordano, A. Grimaud, A. M. Johnson, J. Hwang, E. J. Crumlin, W. Yang, Y. Shao-Horn, *Energy Environ. Sci.* **2017**, *10*, 2190.

[4] Z. W. Seh, J. Kibsgaard, C. F. Dickens, I. Chorkendorff, J. K. Nørskov, T. F. Jaramillo, *Science* **2017**, *355*, eaad4998.

[5] R. F. Savinell, R. L. Zeller, J. A. Adams, *J. Electrochem. Soc.* **1990**, *137*, 489.

[6] K. A. Stoerzinger, M. Risch, B. Han, Y. Shao-Horn, *ACS Catal.* **2015**, *5*, 6021.

[7] C. Wei, S. Sun, D. Mandler, X. Wang, S. Z. Qiao, Z. J. Xu, *Chem. Soc. Rev.* **2019**, *48*, 2518.

[8] F. Song, L. Bai, A. Moysiadou, S. Lee, C. Hu, L. Liardet, X. Hu, *J. Am. Chem. Soc.* **2018**, *140*, 7748.

[9] V. Tripkovic, H. A. Hansen, J. M. Garcia-Lastra, T. Vegge, *J. Phys. Chem. C* **2018**, *122*, 1135.

[10] M. H. Seo, H. W. Park, D. U. Lee, M. G. Park, Z. Chen, *ACS Catal.* **2015**, *5*, 4337.

[11] S. Gupta, W. Kellogg, H. Xu, X. Liu, J. Cho, G. Wu, *Chem. Asian J.* **2016**, *11*, 10.

[12] C. J. Eom, D.-Y. Kuo, C. Adamo, E. J. Moon, S. J. May, E. J. Crumlin, D. G. Schlom, J. Suntivich, *Nat. Commun.* **2018**, *9*, 4034.

[13] J. Scholz, M. Risch, K. A. Stoerzinger, G. Wartner, Y. Shao-Horn, C. Jooss, *J. Phys. Chem. C* **2016**, *120*, 27746.

[14] K. A. Stoerzinger, R. R. Rao, X. R. Wang, W. T. Hong, C. M. Rouleau, Y. Shao-Horn, *Chem* **2017**, *2*, 668.

[15] C. Roy, B. Sebok, S. B. Scott, E. M. Fiordaliso, J. E. Sørensen, A. Bodin, D. B. Trimarco, C. D. Damsgaard, P. C. K. Vesborg, O. Hansen, I. E. L. Stephens, J. Kibsgaard, I. Chorkendorff, *Nat. Catal.* **2018**, *1*, 820.

[16] A. J. Esswein, M. J. McMurdo, P. N. Ross, A. T. Bell, T. D. Tilley, *J. Phys. Chem. C* **2009**, *113*, 15068.

[17] S. Sun, H. Li, Z. J. Xu, *Joule* **2018**, *2*, 1024.

[18] C. Wei, R. R. Rao, J. Peng, B. Huang, I. E. L. Stephens, M. Risch, Z. J. Xu, Y. Shao-Horn, *Adv. Mater.* **2019**, *31*, 1806296.

[19] C. C. L. McCrory, S. Jung, I. M. Ferrer, S. M. Chatman, J. C. Peters, T. F. Jaramillo, *J. Am. Chem. Soc.* **2015**, *137*, 4347.

[20] B. Seo, Y. J. Sa, J. Woo, K. Kwon, J. Park, T. J. Shin, H. Y. Jeong, S. H. Joo, *ACS Catal.* **2016**, *6*, 4347.

[21] E. Locke, S. Jiang, S. K. Beaumont, *Top. Catal.* **2018**, *61*, 977.

[22] D. Antipin, M. Risch, *J. Phys. Energy* **2020**, *2*, 032003.

[23] W. Chen, E. J. G. Santos, W. Zhu, E. Kaxiras, Z. Zhang, *Nano Lett.* **2013**, *13*, 509.

[24] G. Chen, W. Zhou, D. Guan, J. Sunarso, Y. Zhu, X. Hu, W. Zhang, Z. Shao, *Sci. Adv.* **2017**, *3*, e1603206.

[25] K. A. Stoerzinger, M. Risch, J. Suntivich, W. M. Lü, J. Zhou, M. D. Biegalski, H. M. Christen, Ariando, T. Venkatesan, Y. Shao-Horn, *Energy Environ. Sci.* **2013**, *6*, 1582.

[26] A. R. Akbashev, L. Zhang, J. T. Mefford, J. Park, B. Butz, H. Luftman, W. C. Chueh, A. Vojvodic, *Energy Environ. Sci.* **2018**, *11*, 1762.

[27] T. Kosmala, L. Calvillo, S. Agnoli, G. Granozzi, *ACS Catal.* **2018**, *8*, 2343.

[28] L. Jiang, W. S. Choi, H. Jeen, S. Dong, Y. Kim, M.-G. Han, Y. Zhu, S. V. Kalinin, E. Dagotto, T. Egami, H. N. Lee, *Nano Lett.* **2013**, *13*, 5837.

[29] J. D. Baniecki, H. Yamaguchi, C. Harnagea, D. Ricinschi, Z. Gu, J. E. Spanier, T. Yamazaki, H. Aso, *Adv. Energy Mater.* **2019**, *9*, 1803846.

[30] Y. Shi, R. Xie, X. Liu, N. Zhang, C. Aruta, N. Yang, *Phys. Chem. Chem. Phys.* **2019**, *21*, 16230.

[31] K. A. Stoerzinger, W. S. Choi, H. Jeen, H. N. Lee, Y. Shao-Horn, *J. Phys. Chem. Lett.* **2015**, *6*, 487.

[32] J. R. Petrie, V. R. Cooper, J. W. Freeland, T. L. Meyer, Z. Zhang, D. A. Lutterman, H. N. Lee, *J. Am. Chem. Soc.* **2016**, *138*, 2488.

[33] J. Hwang, Z. Feng, N. Charles, X. R. Wang, D. Lee, K. A. Stoerzinger, S. Muy, R. R. Rao, D. Lee, R. Jacobs, D. Morgan, Y. Shao-Horn, *Mater. Today* **2019**, *31*, 100.

[34] A. Grimaud, O. Diaz-Morales, B. Han, W. T. Hong, Y.-L. Lee, L. Giordano, K. A. Stoerzinger, M. T. M. Koper, Y. Shao-Horn, *Nat. Chem.* **2017**, *9*, 457.

[35] J. Liu, E. Jia, K. A. Stoerzinger, L. Wang, Y. Wang, Z. Yang, D. Shen, M. H. Engelhard, M. E. Bowden, Z. Zhu, S. A. Chambers, Y. Du, *J. Phys. Chem. C* **2020**, *124*, 15386.

[36] B. Han, Kelsey A. Stoerzinger, V. Tileli, Andrew D. Gamalski, Eric A. Stach, Y. Shao-Horn, *Nat. Mater.* **2017**, *16*, 121.

[37] J. T. Mefford, W. G. Hardin, S. Dai, K. P. Johnston, K. J. Stevenson, *Nat. Mater.* **2014**, *13*, 726.

[38] D. Kan, Y. Orikasa, K. Nitta, H. Tanida, R. Kurosaki, T. Nishimura, T. Sasaki, H. Guo, Y. Ozaki, Y. Uchimoto, Y. Shimakawa, *J. Phys. Chem. C* **2016**, *120*, 6006.

[39] S. A. Lee, S. Oh, J.-Y. Hwang, M. Choi, C. Youn, J. W. Kim, S. H. Chang, S. Woo, J.-S. Bae, S. Park, Y.-M. Kim, S. Lee, T. Choi, S. W. Kim, W. S. Choi, *Energy Environ. Sci.* **2017**, *10*, 924.

[40] S. H. Chang, N. Danilovic, K.-C. Chang, R. Subbaraman, A. P. Paulikas, D. D. Fong, M. J. Highland, P. M. Baldo, V. R. Stamenkovic, J. W. Freeland, J. A. Eastman, N. M. Markovic, *Nat. Commun.* **2014**, *5*, 4191.

[41] A. Biswas, G. Shiva Shanker, T. Das, R. Mandal, S. Chakraborty, S. Ogale, *Appl. Surf. Sci.* **2020**, *529*, 147065.

[42] I. E. L. Stephens, A. S. Bondarenko, F. J. Perez-Alonso, F. Calle-Vallejo, L. Bech, T. P. Johansson, A. K. Jepsen, R. Frydendal, B. P. Knudsen, J. Rossmeisl, I. Chorkendorff, *J. Am. Chem. Soc.* **2011**, *133*, 5485.

[43] L. Ranno, A. Llobet, R. Tiron, E. Favre-Nicolin, *Appl. Surf. Sci.* **2002**, *188*, 170.

[44] J. Scholz, M. Risch, G. Wartner, C. Luderer, V. Roddatis, C. Jooss, *Catalysts* **2017**, *7*.

[45] L. Chen, Z. Wang, G. Wang, H. Guo, M. Saghayezhian, Z. Liao, Y. Zhu, E. W. Plummer, J. Zhang, *Phys. Rev. Mater.* **2019**, *3*, 044407.

[46] M. Huijben, L. W. Martin, Y. H. Chu, M. B. Holcomb, P. Yu, G. Rijnders, D. H. A. Blank, R. Ramesh, *Phys. Rev. B* **2008**, *78*, 094413.

[47] Z. Liao, N. Gauquelin, R. J. Green, S. Macke, J. Gonnissen, S. Thomas, Z. Zhong, L. Li, L. Si, S. Van Aert, P. Hansmann, K. Held, J. Xia, J. Verbeeck, G. Van Tendeloo, G. A. Sawatzky, G. Koster, M. Huijben, G. Rijnders, *Adv. Funct. Mater.* **2017**, *27*, 1606717.

[48] H. Chen, Y. Yu, Z. Wang, Y. Bai, H. Lin, X. Li, H. Liu, T. Miao, Y. Kou, Y. Zhang, Y. Li, J. Tang, Z. Wang, P. Cai, Y. Zhu, Z. Cheng, X. Zhong, W. Wang, X. Gao, L. Yin, R. Wu, J. Shen, *Phys. Rev. B* **2019**, *99*, 214419.

[49] S. Yousefi Sarraf, S. Singh, A. C. Garcia-Castro, R. Trappen, N. Mottaghi, G. B. Cabrera, C.-Y. Huang, S. Kumari, G. Bhandari, A. D. Bristow, A. H. Romero, M. B. Holcomb, *ACS Nano* **2019**, *13*, 3457.

[50] G. Wan, J. W. Freeland, J. Kloppenburg, G. Petretto, J. N. Nelson, D.-Y. Kuo, C.-J. Sun, J. Wen, J. T. Diulus, G. S. Herman, Y. Dong, R. Kou, J. Sun, S. Chen, K. M. Shen, D. G. Schlom, G.-M. Rignanese, G. Hautier, D. D. Fong, Z. Feng, H. Zhou, J. Suntivich, *Sci. Adv.* **2021**, *7*, eabc7323.

Electrochemically relevant “depth” was characterized by employing epitaxial perovskite oxide heterostructures with atomic-scale precision thickness control. A layer ~10 u.c. (~4 nm) below the surface (electrolyte/electrode interface) was shown to influence the electrocatalytic activity from thickness dependent measurements. Our study redefines the “electrochemical surface” by including the contribution from the sub-surface layers.

Jegon Lee, Prajwal Adiga, Sang A Lee, Seung Hyun Nam, Hyeon-Ah Ju, Min-Hyong Jung, Hu Young Jeong, Young-Min Kim, Cindy Wong, Radwan Elzein, Rafik Addou, Kelsey A. Stoerzinger*, and Woo Seok Choi*

Contribution of the Sub-Surface to Electrocatalytic Activity in Atomically Precise $La_{0.7}Sr_{0.3}MnO_3$ Heterostructures

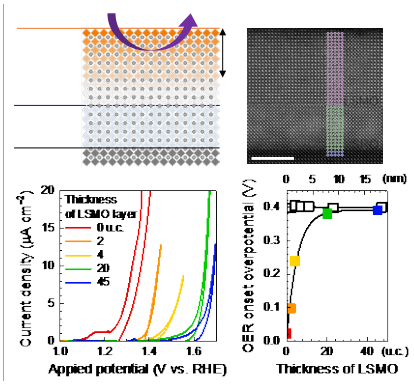

Supporting Information

Contribution of the Sub-Surface to Electrocatalytic Activity in Atomically Precise $La_{0.7}Sr_{0.3}MnO_3$ Heterostructures

Jegon Lee, Prajwal Adiga, Sang A Lee, Seung Hyun Nam, Hyeon-Ah Ju, Min-Hyong Jung, Hu Young Jeong, Young-Min Kim, Cindy Wong, Radwan Elzein, Rafik Addou, Kelsey A. Stoerzinger, and Woo Seok Choi**

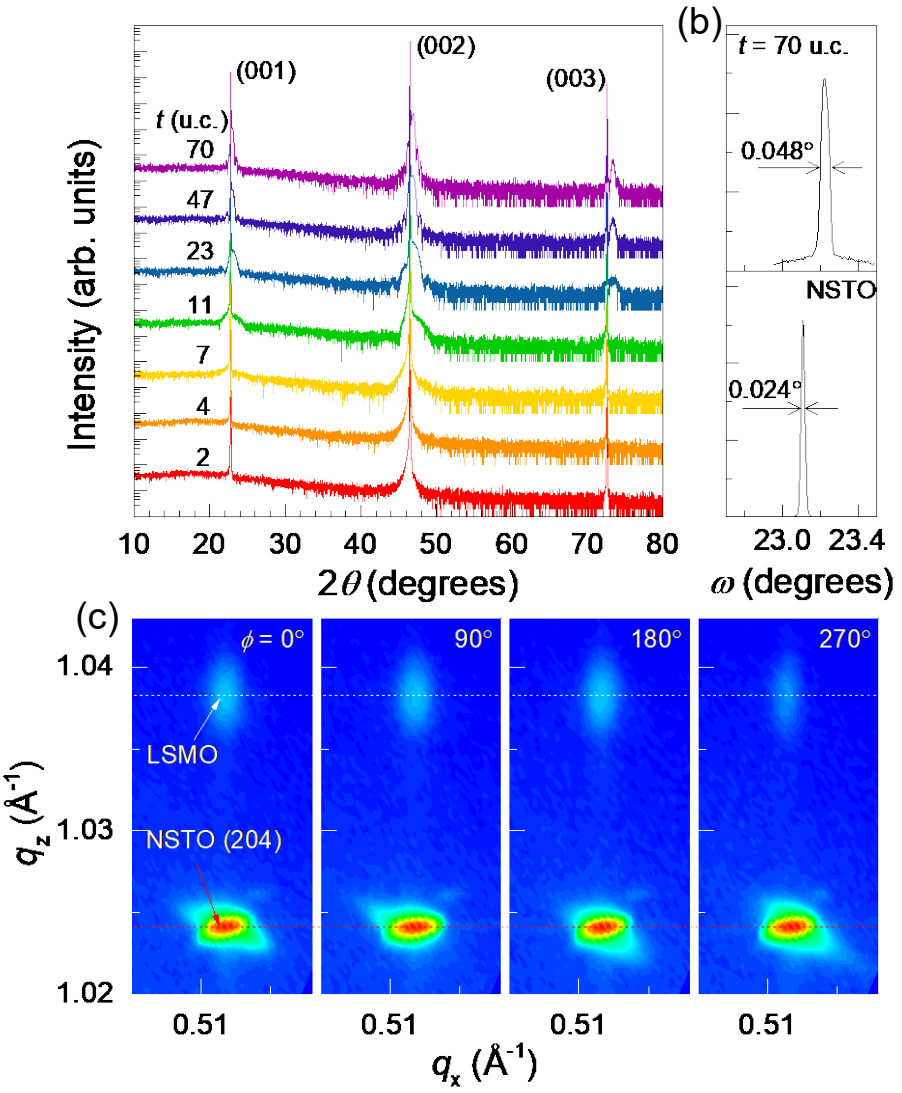

Figure S1. **Lattice structure characterization of the LSMO thin films.** (a) Wide-range XRD θ-2θ scans show high quality epitaxial LSMO thin films without any impurities. (b) XRD rocking-curve scans around (002) Bragg peak of the (thickest) LSMO film and the NSTO substrate, demonstrating the excellent crystalline quality. (c) XRD reciprocal space maps (RSM) of the thickest LSMO film around the substrate NSTO (204) Bragg peak with four orthogonal phi angles. The consistent q_x positions of the LSMO and NSTO (204) peaks indicate that the film is fully strained. The consistent q_z positions of LSMO (204) peaks for the four orthogonal phi angles (0, 90, 180, and 270°) indicate that the LSMO film has a tetragonal crystalline symmetry.

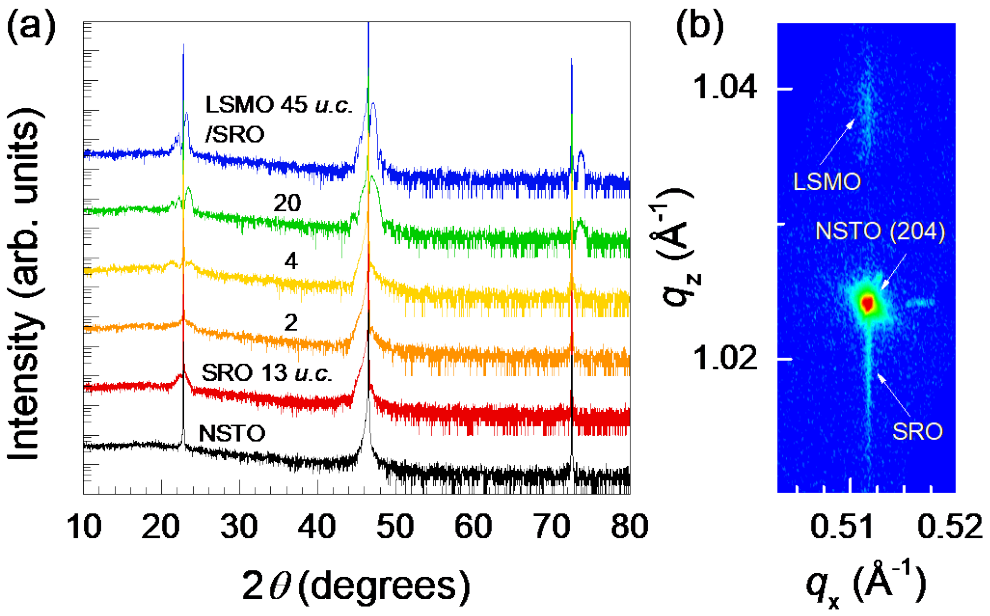

Figure S2. **Lattice structures of the LSMO (*t* u.c.)/SRO (13 u.c.)//NSTO heterostructures.** (a) Wide-range XRD θ-2θ scans show high quality heterostructures without any impurities. (b) The XRD reciprocal space map (RSM) around the substrate NSTO (204) Bragg peak, indicating the fully strained state of the heterostructures for the thickest LSMO layer.

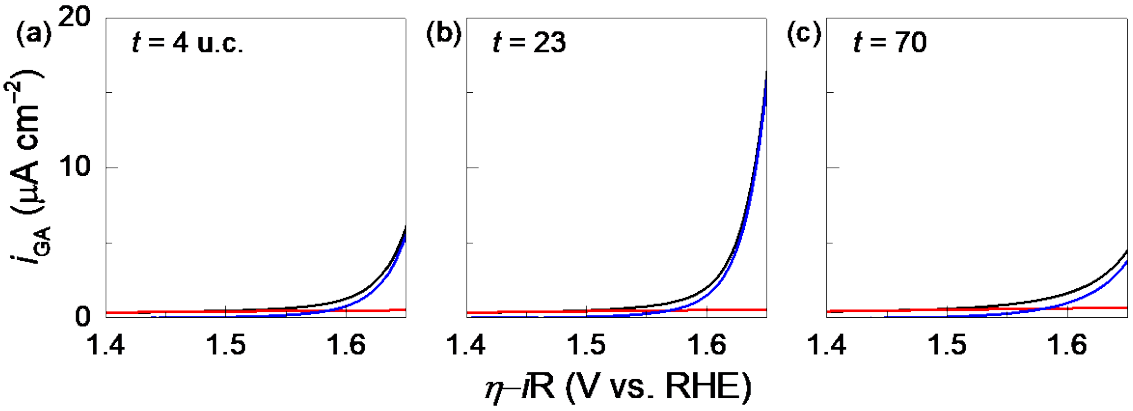

Figure S3. **Exclusion of the capacitive current from the faradaic CV curves.** The capacitive current densities (red line) were estimated using as a linear fitting of the original current densities (black line) in the range of 1.40–1.45 V vs. RHE. Then the capacitive current densities were subtracted from the original current densities, to obtain the CV curves with intrinsic OER effect (blue line). Note that the CV curves were normalized using the GA.

Supplementary Note #1

We estimated electrochemical surface area (ECSA) from the double layer capacitance (C_{dl}) and geometric area (GA) normalized capacitance (c_{dl}) obtained from the average of the forward and reverse scans (Figures S4 and S5, respectively). The obtained c_{dl} values were approximately constant (~110 μF cm^{-2}) across film thickness (4 to 47 u.c.), except for the thinnest (2 u.c.) and the thickest (70 u.c.) films. ECSA was obtained by dividing C_{dl} by specific capacitance of conventional smooth oxide surface (40 μF cm^{-2}),[1] of which the results are summarized in Table S1. The surface roughness factors R_f are in the range of 2 and 3, comparable to the electrochemically smooth surface.[1-3] The comparable capacitance for films 4 to 47 u.c. in thickness indicates that the LSMO films have consistent full-coverage of the substrate, also evidenced by the smooth film surface from atomic force microscopy (Figure S6).

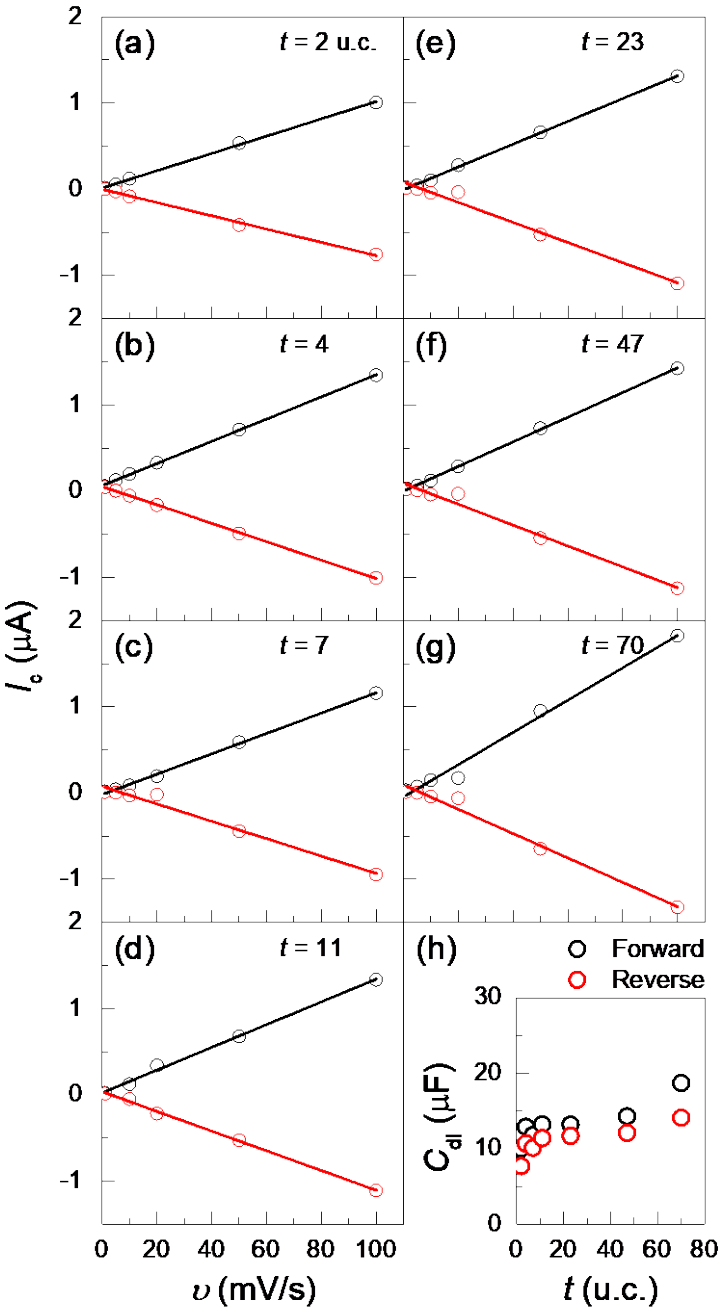

Figure S4. **Electrochemical double layer capacitance (C_{dl}) for the LSMO films with different thickness.** (a)-(g) Linear charging currents (I_c) with the different scan rates (υ) within the non-faradaic potential region (~1.0 V vs. RHE). (h) The double layer capacitance (C_{dl}) for the thin films with different thicknesses were obtained from the linear slopes of the plots in (a)-(g).

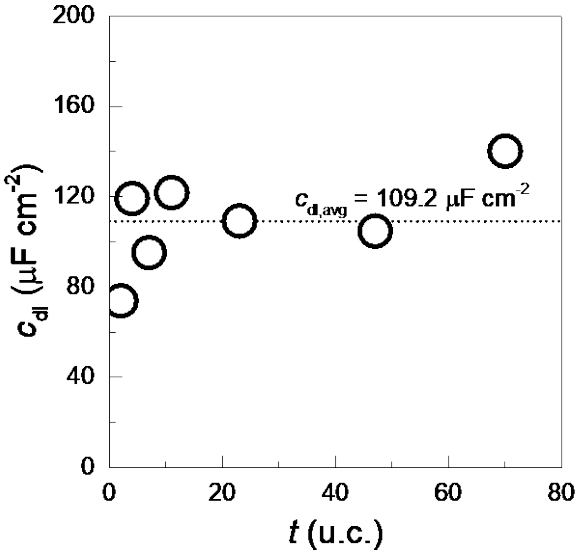

Figure S5. **Normalized double layer capacitance (c_{dl}).** The double layer capacitances were normalized via exposed geometric area of working electrode, sample-by-sample. The dotted line indicates the average value of c_{dl}, consistent with the reported value.[1-3]

t (u.c.)	C_{dl} (μF)			ECSA using 40 μF cm^{-2} (cm^2)	GA (cm^2)	R_f
	Forward	Reverse	Average	Average		
2	10.0	7.70	8.85	0.222	0.120	1.85
4	12.9	10.7	11.8	0.295	0.099	2.98
7	11.8	10.1	11.0	0.274	0.115	2.38
11	13.2	11.4	12.3	0.308	0.101	3.05
23	13.2	11.7	12.5	0.311	0.114	2.73
47	14.3	12.1	13.2	0.330	0.126	2.62
70	18.7	14.1	16.4	0.410	0.117	3.50

Table S1. **Surface roughness factors for the LSMO thin films with different thicknesses.** The ECSA was determined by the specific capacitance of conventional smooth oxide surface (40 μF cm^{-2}). Also, GA indicates the actual electrode area exposed to the electrolyte, and the roughness factor (R_f) was determined by the following equation, $R_f = \frac{\text{ECSA}}{\text{GA}}$.

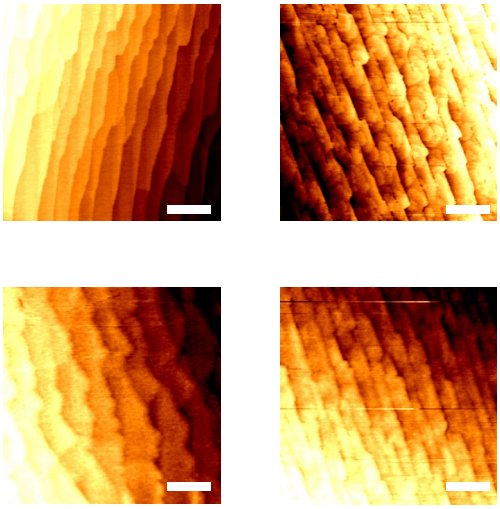

Figure S6. Surface roughness and layer-by-layer growth of the films using atomic force microscopy. The surface morphologies for the (a) NSTO substrate, (b) LSMO ~30 nm // NSTO, (c) SRO ~5 nm // NSTO, and (d) LSMO ~10 nm / SRO 5 nm // NSTO samples. All the samples show the layer-by-layer growth and similar surface roughness in which root-mean-squared roughness is less than the step height of the LSMO u.c. (= ~0.4 nm). The scale bars indicate 1 μm.

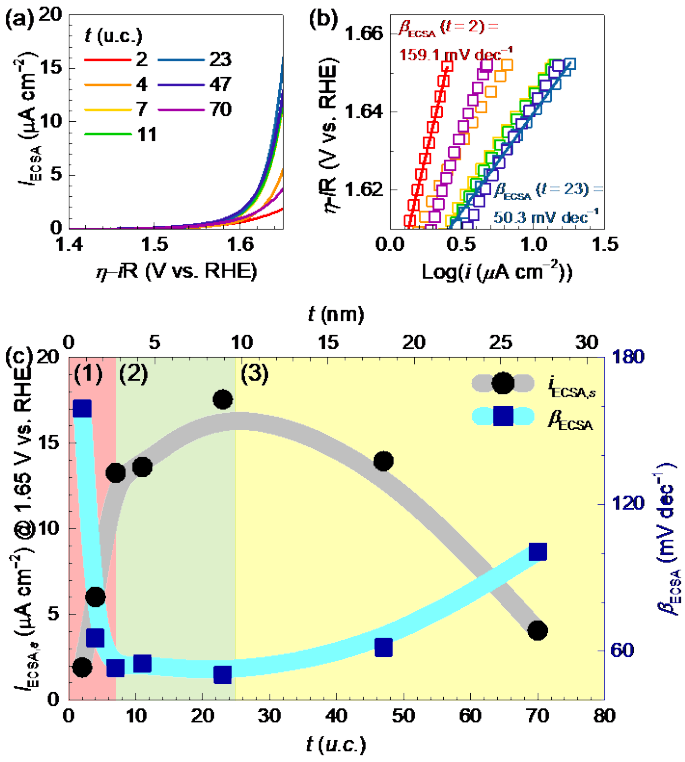

Figure S7. *t*-dependent oxygen evolution reaction normalized by ECSA. (a) OER cyclic voltammetry and (b) its Tafel plots with normalizing by the ECSA. (c) The summary of the specific current densities of the OER ($i_{ECSA,s}$) at a potential of 1.65 V vs. RHE (left axis) and Tafel slopes of the OER (β_{ECSA}) (right axis) as a function of *t*. The *t*-dependent activity trends are qualitatively the same the results using GA normalization. Regions (1), (2) and (3) are marked as red, green, and yellow, respectively.

Supplementary Note #2

The Tafel slope values (β) were obtained from Tafel equation, $\eta_{ov} = \beta \times \log\frac{i}{i_0}$, where η_{ov}, β, i, and i_0 are the overpotential, Tafel slope, current density, and exchange current density, respectively.

t **(u.c.)**	**Specific current density (i_s, μA cm^{-2}) @ 1.65 V vs. RHE**	**Onset overpotential (η_{on}, V)**	**Tafel slope (β, mV dec^{-1})**
2	3.4	0.398	109.0
4	16.2	0.405	56.4
7	27.7	0.402	49.3
11	36.8	0.402	49.9
23	42.7	0.398	47.4
47	33.6	0.400	55.2
70	13.0	0.403	82.9

Table S2. The OER activity parameters of the LSMO thin films from Figure 3.

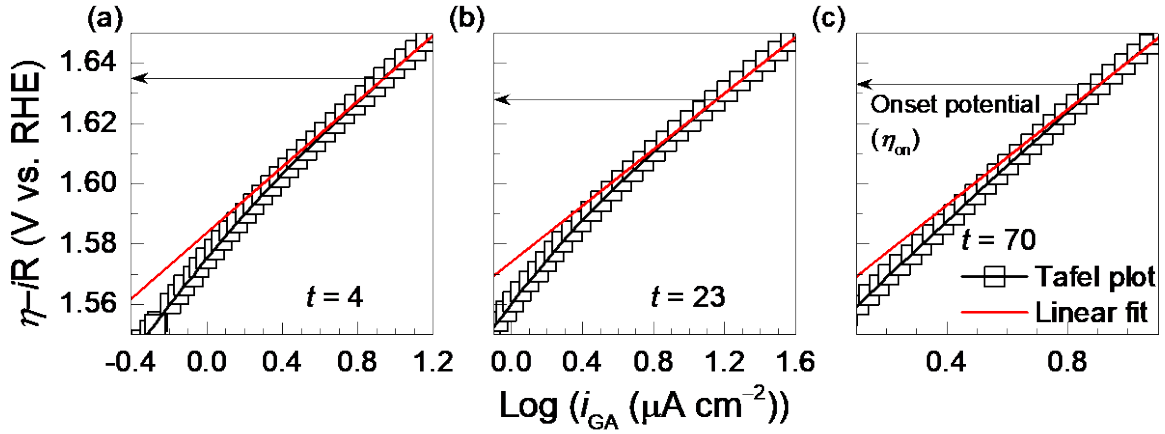

Figure S8. Determination of the OER onset potential. The Tafel plots of the LSMO thin films in the (a) thin-, (b) intermediate-, and (c) thick-regions. The onset potentials were determined by identifying the point where the Tafel curve (black) deviates from the linear fit line (red), by more than the standard deviation of the linear fitting.

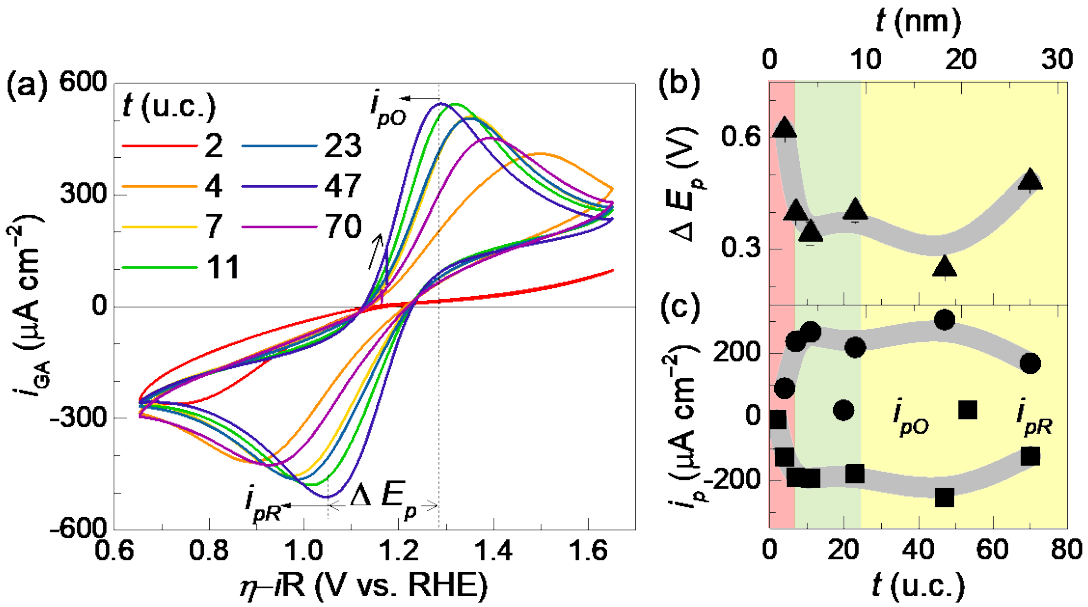

Figure S9. Redox reactions in the LSMO thin films. (a) Cyclic voltammetry performed in electrolyte of 5 mM $K_3[Fe(CN)]_6$ + 5 mM $K_4[Fe(CN)]_6$ + 0.1 M KOH. To determine the electrocatalytic activities of the LSMO films, (b) separation of the potentials (ΔE_p) between the peaks, and (c) peak heights of the oxidation and reduction reactions (i_{pO} and i_{pR}) were plotted. In (b) and (c) the 2 u.c. film is omitted due to the lack of oxidation peak from the formation of a dead layer with high charge transfer resistance.

***t* (u.c.)**	**Peak separation (V)**						
	Cycle 2	3	4	5	6	Avg.	Stn. dev.
2							
4	0.632	0.625	0.618	0.615	0.612	0.620	0.0080
7	0.419	0.405	0.395	0.388	0.382	0.398	0.0144
11	0.388	0.355	0.339	0.321	0.308	0.342	0.0312
23	0.444	0.414	0.394	0.384	0.371	0.402	0.0286
47	0.244	0.244	0.244	0.251	0.251	0.247	0.0036
70	0.497	0.487	0.480	0.473	0.470	0.482	0.0107

Table S3 | Peak separations of the ferri/ferrocyanide redox reaction couple.

t (u.c.)	Oxidation peak height (μA cm^{-2})						
	Cycle 2	3	4	5	6	Avg.	Stn. dev.
2							
4	81.6	87.3	92.0	92.1	94.2	89.5	4.53
7	226.5	235.7	238.4	243.0	240.5	236.8	5.68
11	206.4	222.8	229.0	240.1	273.8	234.4	22.51
23	212.0	237.2	251.8	261.8	264.2	245.4	19.21
47	337.0	337.6	337.5	336.9	335.8	337.0	0.64
70	155.4	163.1	165.8	169.4	185.0	167.7	9.77

Table S4 | Oxidation peak heights of the ferri/ferrocyanide redox reaction couple.

t (u.c.)	Reduction peak height (μA cm^{-2})						
	Cycle 2	3	4	5	6	Avg.	Stn. dev.
2	−4.9	−7.6	−9.6	−11.2	−12.2	−9.1	2.60
4	−121.2	−123.5	−127.9	−129.6	−128.0	−126.0	3.14
7	−182.5	−185.0	−192.0	−195.2	−198.7	−190.7	6.08
11	−155.0	−162.4	−172.1	−178.1	−180.0	−169.5	9.51
23	−184.1	−192.2	−200.7	−205.9	−219.6	−200.5	12.12
47	−279.8	−278.9	−280.1	−280.9	−281.9	−280.3	1.01
70	−116.3	−120.7	−127.0	−125.0	−127.8	−123.4	4.30

Table S5 | Reduction peak heights of the ferri/ferrocyanide redox reaction couple.

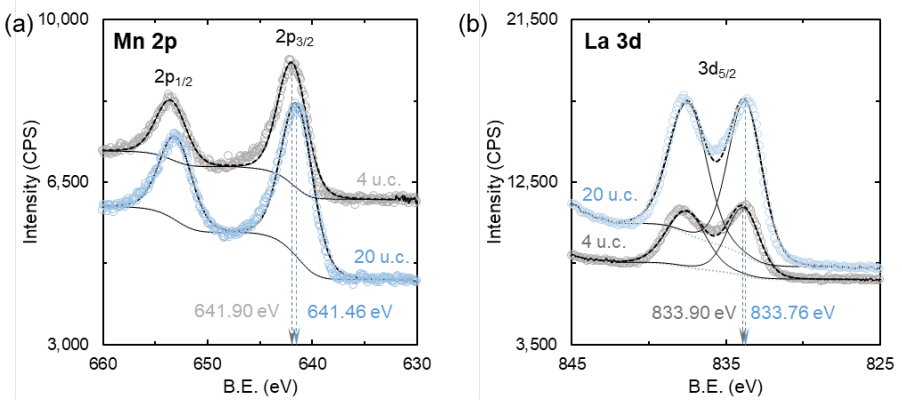

Figure S10 | XPS results on the LSMO/SRO//NSTO heterostructures. High resolution (a) Mn 2*p* and (b) La 3*d* spectra of LSMO (4 u.c.)/SRO//NSTO and (20 u.c.)/SRO//NSTO post-cycling, suggests higher Mn/La ratio for 4 u.c. film possibly linked to Sr segregation at the LSMO/SRO interface while the Mn/La ratio for 20 u.c. film is close to the expected ratio, for a stable LSMO/SRO layer.

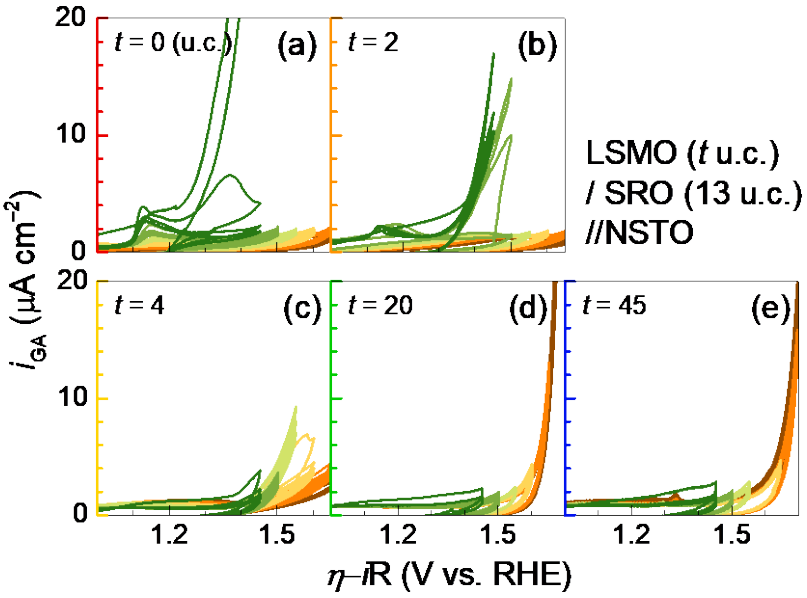

Figure S11 | The OER CV curves for the LSMO/SRO//NSTO heterostructures. (a-e) Cyclic voltammetry curves with incrementally increasing maximum potentials, i.e., 1.45, 1.50, 1.55, 1.60, 1.65, and 1.70 V vs. RHE, for heterostructures with t = 0-45.

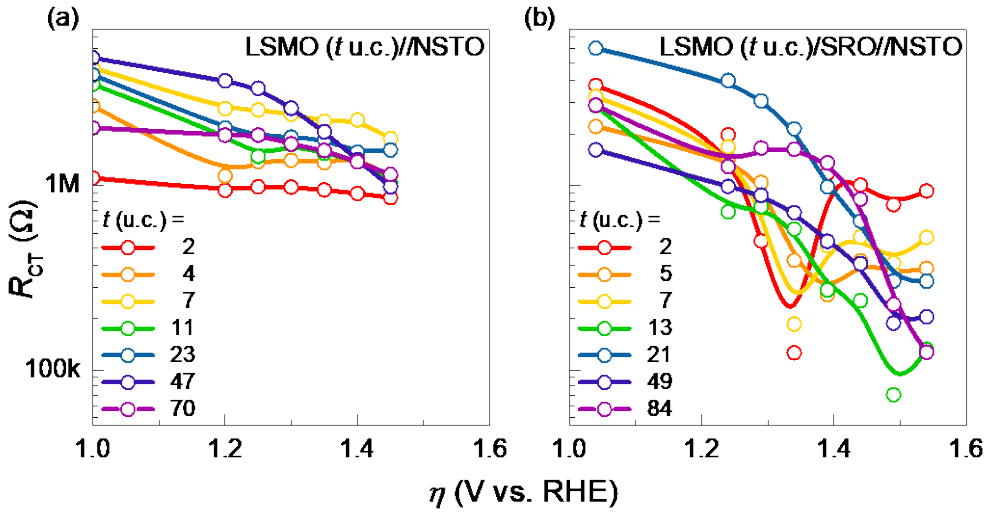

Figure S12 | The contribution of the buried SRO layer on the OER activity from the charge transfer resistance. The charge transfer resistance (R_{CT}) of the LSMO thin films on the (a) NSTO and (b) SRO covered NSTO were determined by the potentiostatic electrochemical impedance spectroscopy.

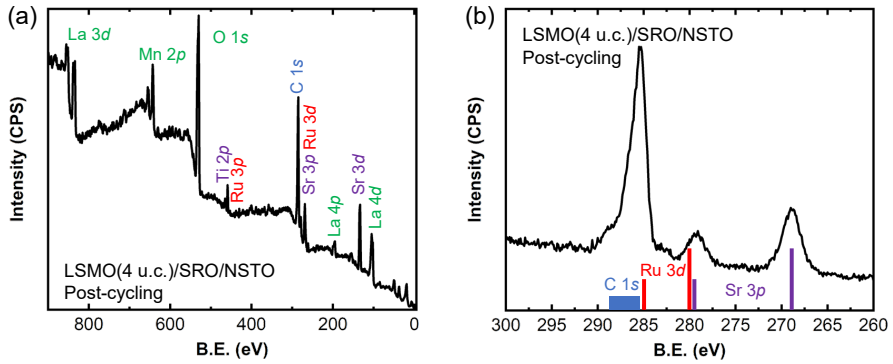

Figure S13 | XPS results on the LSMO/SRO//NSTO heterostructures. a) Survey spectrum of LSMO (4 u.c.)/SRO//NSTO after cycling, showing the LSMO film remains present on the surface. b) High resolution scan in the binding energy region of the C 1*s*, Ru 3*d*, and Sr 3*p* core levels.

References

[1] C. C. L. McCrory, S. Jung, I. M. Ferrer, S. M. Chatman, J. C. Peters, T. F. Jaramillo, *J. Am. Chem. Soc.* **2015**, *137*, 4347.

[2] J. Scholz, M. Risch, K. A. Stoerzinger, G. Wartner, Y. Shao-Horn, C. Jooss, *J. Phys. Chem. C* **2016**, *120*, 27746.

[3] Y. Qiu, J. A. Lopez-Ruiz, U. Sanyal, E. Andrews, O. Y. Gutiérrez, J. D. Holladay, *Appl. Catal. B* **2020**, *277*, 119277.